Solar Energy 300 (2025) 113788

Contents lists available at ScienceDirect

Solar Energy

journal homepage: www.elsevier.com/locate/solener

Theoretical investigation of high-efficiency halide perovskite $Rb_2NaTlBr_6$ for photovoltaic solar cells

M. Agouri [a], H. Fatihi [a], H. Ouhenou [a], N. Khossossi [b], A. Abbassi [a,*], S. Taj [a], B. Manaut [a,*]

[a] Laboratory of Research in Physics and Engineering Sciences, Sultan Moulay Slimane University, Polydisciplinary Faculty, Beni Mellal, 23000, Morocco
[b] Department of Materials Science and Engineering, Faculty of Mechanical, Maritime and Materials Engineering, Delft University of Technology, Mekelweg 2, Delft, 2628 CD, The Netherlands

ARTICLE INFO

Keywords:
Double halide perovskites
Density functional theory (DFT)
Photovoltaic materials
Spectroscopic limited maximum efficiency (SLME)

ABSTRACT

The development of stable, non-toxic, and high-efficiency perovskite materials is critical for advancing next-generation photovoltaic technologies. While numerous halide double perovskites have been explored, many suffer from indirect band gaps or limited optoelectronic tunability. In this work, we employ first principles calculations to investigate the structural, electronic, and optical characteristics of the rubidium-based double perovskite $Rb_2NaTlBr_6$. Our results reveal that the compound exhibits a direct band gap of 1.869 eV, along with strong, dynamic and thermodynamic stability. Notably, the application of tensile strain engineering systematically reduces the band gap to 1.374 eV, placing it within the optimal range for solar absorption and significantly enhancing its optoelectronic response. The material also demonstrates high absorption coefficients and favorable carrier effective masses. Importantly, the spectroscopic limited maximum efficiency (SLME) reaches 33% under 5% tensile strain, underscoring its photovoltaic potential. The findings suggest that strain engineered $Rb_2NaTlBr_6$ is promising, lead-free candidate for high-efficiency solar energy applications.

1. Introduction

With the environmental challenges posed by fossil fuels and the global shift towards renewable energy [1,2], solar cell technology has emerged as a prominent and robust solution for capturing solar radiation to generate electricity [3]. It plays a crucial role in promoting eco-friendly energy practices while supporting sustainable economic and social development that impacts many aspects of human life [4]. Although silicon remains the dominant material in commercial photovoltaic technology, it faces several significant drawbacks, including limited efficiency, high manufacturing costs, and complex processing requirements [5]. Hence, developing advanced solar cell materials that offer enhanced energy efficiency and cost effectiveness is essential, aiming to eventually replace silicon based technologies.

Among emerging alternatives, perovskite materials have garnered significant interest for their remarkable optoelectronic properties [6,7]. Since 2009, the power conversion efficiency (PCE) of perovskite solar cells has rapidly increased from 3.8 to 25.7% by 2021 [8]. However, traditional lead-based hybrid halide perovskites are plagued by two major issues, including chemical instability and the toxicity of lead, which raises serious environmental and health concerns [9–14]. These drawbacks have motivated researchers to explore lead-free alternatives, with halide double perovskites (HDPs) emerging as highly promising candidates for developing stable and non-toxic solar absorber materials [15]. Halide double perovskite materials, which adopt the general chemical formula $A_2BB'X_6$ (where A is a monovalent cation, B and B' are monovalent and trivalent metal cations, and X is a halide), offer a structurally stable and environmentally friendly alternative to lead-based perovskites [16,17]. Their tunable electronic structures, high optical absorption, long carrier diffusion lengths, and high defect tolerance make them ideal for photovoltaic applications [18–21]. Compounds such as $Cs_2AgBiBr_6$ and $Cs_2BiAgCl_6$ have been extensively studied for their favorable optoelectronic characteristics [22]. Although many HDPs possess indirect band gaps that can reduce light-harvesting efficiency, strategic chemical substitution, lattice strain engineering, and dimensional control have been employed to modify their band structures, promoting more favorable direct band gap behavior [23,24]. The research on HDPs has significantly expanded, encompassing both theoretical and experimental investigations. In particular, compound-type $Cs_2AgBiBr_6$ has demonstrated excellent optical properties and photostability, making them strong candidates for practical solar cell applications [25]. Moreover, first-principles calculations have also highlighted a range of promising inorganic halide double perovskites, such as Cs_2ABI_6 (AB:GeZn, SnBe) and Rb_2AgBiX_6 (X=Cl, Br, I), which exhibit tunable band gaps, low effective masses, and

* Corresponding authors.
E-mail addresses: abbassi.abder@gmail.com (A. Abbassi), b.manaut@usms.ma (B. Manaut).

https://doi.org/10.1016/j.solener.2025.113788
Received 19 February 2025; Received in revised form 17 June 2025; Accepted 11 July 2025
Available online 26 July 2025

high solar absorption coefficients. These characteristics further underscore their potential suitability for clean technologies, particularly solar cells [26,27]. Additionally, thallium-containing halide double perovskites, such as Rb_2TlSbX_6 (X=Cl, Br, I) and $Cs_2AgTlBr_6$, have gained attention due to their remarkable optoelectronic performance [28,29]. Despite concerns regarding Tl toxicity, recent experimental works have demonstrated that $Cs_2AgTlBr_6$ exhibits microsecond carrier lifetimes and carrier diffusion lengths exceeding 1 μm, even under trap-limited conditions. This indicates that with proper surface passivation and synthesis control, Tl-based halide double perovskites can achieve defect tolerance and photovoltaic performance comparable to, or surpassing that of lead-based systems [29]. For instance, H. Fatihi et al. reported that $Rb_2TlAsBr_6$ could achieve a spectroscopic limited maximum efficiency (SLME) of up to 31.4% [30]. Similarly, Rb_2AgBiX_6 (X=Cl, Br, I) compounds have shown SLME values ranging from 24 to 30%, indicating strong photovoltaic potential [27].

Motivated by these remarkable advances and the distinctive photovoltaic properties exhibited by this material family, we present a comprehensive theoretical investigation of $Rb_2NaTlBr_6$ as a promising candidate for high-performance solar cell applications. Our systematic study employs state-of-the-art density functional theory calculations, incorporating the modified Becke–Johnson potential and spin–orbit coupling effects, combined with the SLME method to evaluate its photovoltaic potential. We demonstrate that strategic application of tensile strain engineering can optimize the electronic band structure, resulting in enhanced optical absorption and improved charge transport properties. Our findings reveal that $Rb_2NaTlBr_6$ exhibits exceptional potential for photovoltaic applications, with theoretical predictions suggesting performance metrics that could exceed those of currently known double halide perovskites.

2. Computational details

We performed first-principles calculations to investigate the structural stability, optoelectronic properties, and carrier transport characteristics of the cubic inorganic halide double perovskite $Rb_2NaTlBr_6$. All calculations were executed using the FP-LAPW method [31] within density functional theory (DFT), as implemented in the WIEN2k code [32,33]. The structural optimization and stability analysis were conducted using the Generalized Gradient Approximation with the Perdew–Burke–Ernzerhof functional (GGA-PBE) [34]. For electronic structure calculations, we employed three different approaches: standard GGA, the modified Becke–Johnson potential (mBJ), HSE06, and mBJ combined with spin–orbit coupling (mBJ+SOC). These calculations were performed both with and without strain effects. The mBJ approach yielded band gap values that showed excellent agreement with previous theoretical and experimental findings [34–37], and was therefore selected for subsequent optical and transport property calculations [37,38]. Throughout all calculations, we maintained consistent computational parameters: the angular momentum expansion up to $l_{max} = 10$, the plane-wave cutoff parameter $RMT \times K_{max} = 7$, and the charge density Fourier expansion $G_{max} = 12$. The Brillouin zone integration was performed using a 600 k-point mesh in the irreducible wedge, ensuring convergence of the electronic properties.

To investigate the effects of tensile strain engineering on unit cell dimensions, we applied strain ranging from 0 to 5% in 1% increments. The applied strain is defined by the following equation [39]:

$$strain(\%) = \frac{a - a'}{a} \times 100 \tag{1}$$

where a' and a are the lattice constants strained and unstrained structures, respectively.

3. Results and discussion

3.1. Theoretical stability

The double halide perovskite $Rb_2NaTlBr_6$ crystallizes in an ideal cubic structure with space group $Fm\bar{3}m$. The optimized crystal structure is illustrated in Fig. 1(a). The unit cell consists of four crystallographically distinct atomic positions: Rb, Na, Tl, and Br atoms occupying the positions $(\frac{3}{4}, \frac{3}{4}, \frac{1}{4})$, $(\frac{1}{2}, 0, 0)$, $(0, 0, 0)$, and $(0.24, 0, 0)$, respectively. The optimized lattice parameter obtained from our calculations is presented in Table 1, alongside values from previous theoretical studies. Our computed structural parameters demonstrate excellent agreement with previously reported literature values [40], validating the reliability of our computational methodology. The observed variations in lattice constants compared to related perovskite compounds such as $Rb_2LiTlBr_6$ and $Cs_2NaTlBr_6$ can be rationalized through the differences in ionic radii of the constituent atoms [41,42]. This structural configuration provides an optimal framework for the unique electronic and optical properties discussed in subsequent sections.

Theoretical stability assessments play a fundamental role in advancing our understanding the potential of this material for high performance applications, such as solar cells and optoelectronic [43]. For this reason, we assessed the theoretical stability of $Rb_2NaTlBr_6$ by calculating its tolerance and octahedra factors, cohesive and formation energies, as well as its phonon dispersion. The theoretical tolerance (τ/t) and octahedra (μ) factors were computed using the following equations [44–46]:

$$\tau = \frac{R_{Br}}{R_B} - n_{Rb}\left(n_{Rb} - \frac{\frac{R_{Rb}}{R_B}}{ln\left(\frac{R_{Rb}}{R_B}\right)}\right);$$

$$t = \frac{R_{Rb} + R_{Br}}{\sqrt{2}(R_B + R_{Br})}; \tag{2}$$

$$\mu = \frac{R_{Na} + R_{Tl}}{2R_{Br}}$$

where $R_{i=Rb,Na,Tl,Br}$ represents the ionic radii of each ion and the n_{Rb} is the oxidation state of Rb. Table 1 shows that the calculated t, τ, and μ factors meet Goldschmidt's conditions ($0.8 < t < 1.1$, $\tau < 4.18$, and $\mu > 0.41$), fulfilling the stability and formation of studied compound in its ideal cubic structure [44–46]. The thermodynamic stability of the studied halide perovskite was evaluated by calculating its formation and cohesive energies, using the following equations:

$$\Delta H_f(eV/atom) = \frac{E_{tot}(Rb_2NaTlBr_6) - (2E_{Rb}^{Bulk} + E_{Na}^{Bulk} + E_{Tl}^{Bulk} + 6E_{Br}^{Bulk})}{10} \tag{3}$$

$$E_{coh}(eV/atom) = \frac{E_{tot}(Rb_2NaTlBr_6) - (2E_{Rb}^{Gas} + E_{Na}^{Gas} + E_{Tl}^{Gas} + 6E_{Br}^{Gas})}{10} \tag{4}$$

where $E_{tot}(Rb_2NaTlBr_6)$ represents the total energy of $Rb_2NaTlBr_6$ perovskite. $R_{i=Rb,Na,Tl,Br}^{Bulk/Gas}$ represents the total energy of each atom in its bulk/gaseous forms, respectively. The calculated formation and cohesive energies are found to be −2.83 and −2.40 eV/atom, respectively, ensuring the thermodynamic stability of studied compound. This formation energy value is consistent with the range of formation energies computed for other halide perovskite materials, both experimentally and theoretically studied, such as $Rb_2LiTlBr_6$, $Cs_2NaTlBr_6$ and others [40,42,47].

Additionally, the dynamical stability of the cubic $Rb_2NaTlBr_6$ structure was examined through the phonon dispersion curve, as depicted in Fig. 1(b). The absence of any imaginary frequency modes along

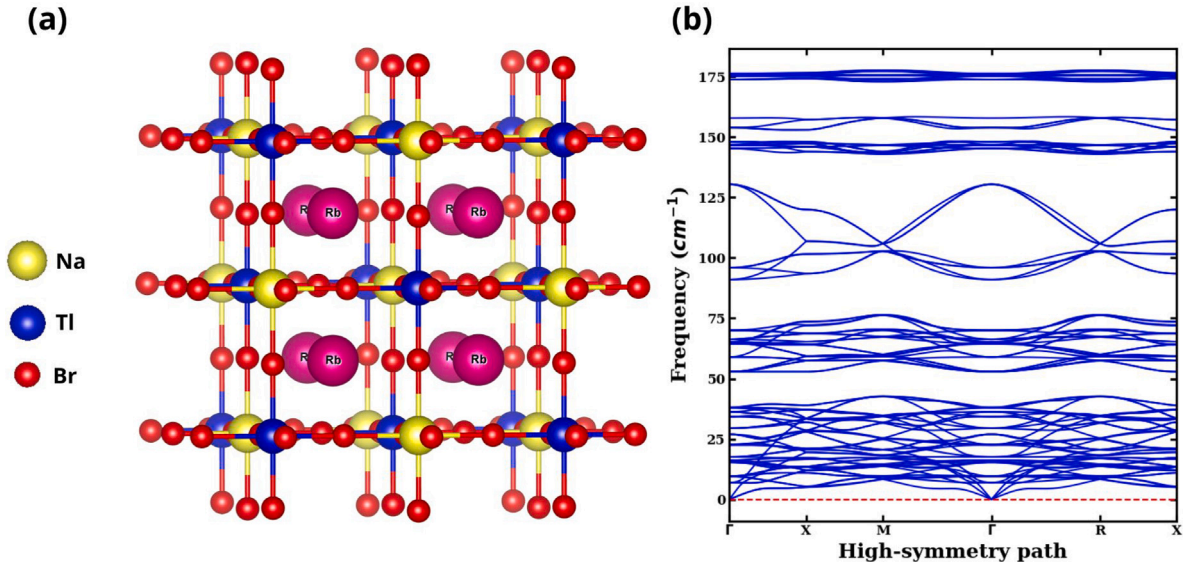

Fig. 1. Crystal structure (a) and phonon dispersion (b) of cubic $Rb_2NaTlBr_6$ perovskite.

Table 1
Calculated structural parameters, tolerance factors (t and τ), and octahedra factor (μ), as well as cohesive (E_c) and formation (ΔH_f) energies of cubic $Rb_2NaTlBr_6$ along with other halide double perovskites for comparison.

Compound	a (Å)	τ	t	μ	ΔH_f (eV/atom)	E_{coh} (eV/atom)	Bulk modulus (B)	Pressure derivative (B')
$Rb_2NaTlBr_6$	11.40	4.11	0.90	0.49	−2.61	−2.40	19.8069	6.0139
$Rb_2NaTlBr_6$ [40]	11.39		0.87		−1.77			
$Rb_2LiTlBr_6$ [42]	11.11		0.94		−2.00			
$Cs_2NaTlBr_6$ [41]	11.13							

the high symmetry path of the first Brillouin zone (BZ) confirms the dynamical stability of $Rb_2NaTlBr_6$ perovskite. Based on these findings, we can conclude that the cubic $Rb_2NaTlBr_6$ perovskite demonstrates excellent theoretical stability, favoring its potential for experimental synthesis and advanced technology applications.

3.2. Electronic properties

3.2.1. Band structure

The electronic properties of semiconductor materials, particularly their band gap energies, are fundamentally determined by atomic orbital contributions across the valence-conduction band transition. We performed comprehensive DFT calculations to elucidate the electronic structure of $Rb_2NaTlBr_6$, focusing on band structure analysis and density of state distributions (both total and orbital-resolved). This detailed electronic structure characterization provides crucial insights into the material's potential for photovoltaic applications, including its light-harvesting capabilities and charge transport mechanisms.

The calculated band gap energies using various theoretical approaches are summarized in Table 2 . All computational methods consistently predict semiconducting behavior for $Rb_2NaTlBr_6$. The PBE-GGA approach yields a band gap of 0.788 eV, while the mBJ potential provides an improved description of the electronic structure, effectively addressing the well-known band gap underestimation inherent to standard GGA functionals. The mBJ-computed band gap demonstrates excellent agreement with previous theoretical investigations [40]. Notably, the inclusion of SOC effects within the mBJ framework, as well as the application of the HSE06 approach, results in negligible band gap modification, introducing changes of only 10^{-3} eV. Given this minimal impact, SOC effects were omitted from subsequent calculations to optimize computational efficiency [48]. Fig. 2 presents the electronic band structure of $Rb_2NaTlBr_6$ along high-symmetry directions in the first Brillouin zone, calculated using the mBJ approach. The band

Table 2
Calculated band gap energy of cubic $Rb_2NaTlBr_6$ using different approaches.

Compound	Method	Band gap E_g (eV)
$Rb_2NaTlBr_6$	PBE	0.788; 0.91 [40]
	PBE+mBJ	1.869; 1.87 [40]
	PBE+mBJ+SOC	1.865
	HSE06	1.756

structure analysis reveals that both the valence band maximum (VBM) and conduction band minimum (CBM) are located at the Γ-point, confirming the direct nature of the fundamental band gap. This direct gap characteristic, combined with the optimal band gap energy, positions $Rb_2NaTlBr_6$ as a promising candidate for efficient photovoltaic and optoelectronic applications.

3.2.2. Density of states

To elucidate the orbital character of electronic states and understand the microscopic origin of the band structure features, we analyzed the total and partial density of states of $Rb_2NaTlBr_6$, as presented in Fig. 3. The DOS analysis reveals that the electronic structure is predominantly characterized by Br p-orbital contributions across the entire energy spectrum, with particularly significant contributions to the CBM states near the Fermi level. A notable feature is the strong hybridization between Tl-p and Br-p states in the vicinity of the Fermi level, indicating that these orbitals play a crucial role in determining the fundamental band gap of $Rb_2NaTlBr_6$.

The DOS shows higher density of states in the VBM region near the Fermi level compared to the CBM, suggesting favorable conditions for electronic transitions. The alkali metals, Rb and Na, exhibit minimal contributions to the states near the Fermi level, primarily serving to stabilize the perovskite crystal structure through charge donation.

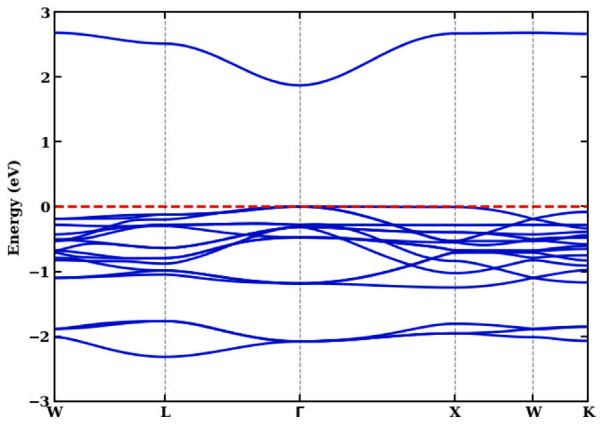

Fig. 2. Electronic band structure of the $Rb_2NaTlBr_6$ perovskite using PBE+mBJ functional.

Table 3
Calculated band gap energy of $Rb_2NaTlBr_6$ perovskite under varying tensile strains using the mBJ approach, along with the lattice parameter and formation energy.

Compound	*strain* (%)	E_g (eV)	a (Å)	ΔH_f (eV/atom)
Rb2NaTlBr6	0	1.869	11.40	−2.61
	1	1.764	11.51	−2.60
	2	1.663	11.63	−2.59
	3	1.564	11.74	−2.58
	4	1.458	11.86	−2.57
	5	1.374	11.97	−2.56

This electronic structure characteristic is consistent with other double halide perovskites, where alkali metal cations primarily contribute to structural stability rather than participating directly in electronic transitions [49]. The pronounced p-orbital character of both occupied and unoccupied states, primarily derived from Br and Tl contributions, confirms the *p*-type semiconducting nature of $Rb_2NaTlBr_6$. This finding aligns with recent investigations of electronic properties in similar double halide perovskite systems [40], suggesting potential applications in p-type semiconductor devices.

3.2.3. Strain effect

Optimizing the band gap energy is significant for enhancing the efficiency and performance of photovoltaic (PV) materials. The Shockley–Queisser (SQ) limit indicates that the ideal band gap energy for a single p–n junction solar cell is approximately 1.34 eV, corresponding to a theoretical maximum efficiency of about 33.7% [50]. This ideal band gap value represents the optimal balance among various optoelectronic properties, including the absorption coefficient, ensuring that the material can convert the maximum fraction of incident solar energy into electrical power. Therefore, materials with band gaps close to this optimal value of 1.34 eV are highly desirable for achieving peak performance and efficiency in PV applications.

In our study, the computed band gap value of $Rb_2NaTlBr_6$ using mBJ approach is of about 1.869 eV. To approach the optimal band gap value predicted by the Shockley–Queisser limit, we investigated the effect of tensile strain engineering on the $Rb_2NaTlBr_6$ perovskite. As shown in Table 3, the applied tensile strain increases the lattice constant of the cubic $Rb_2NaTlBr_6$ structure. This structural modification leads to a reduction in the band gap, which can enhance optical absorption and photovoltaic efficiency. Mechanical strain has been widely recognized as an effective method to tune the optoelectronic properties of perovskite materials. For instance, B. Rezini et al. [51] demonstrated that tensile strain reduces the band gap and modifies carriers mobility in Cs_2SnI_6 double halide perovskite, while compressive strain has the opposite effect. Similarly, strain-induced band gap tuning and enhanced optical absorption were reported for Cs_2InSbX_6 (X = F, Cl) perovskites by S. Tariq et al. [52]. These findings support our approach by applying up to 5% tensile strain engineering to optimize $Rb_2NaTlBr_6$ for solar cell applications. In addition, to confirm the intrinsic thermodynamic stability of $Rb_2NaTlBr_6$ under strained conditions, we calculated the formation energy. Our results show a negative formation energy, indicating that the system is stable and not prone to structural degradation even under tensile strain. This further validates the feasibility of strain engineering in this material without compromising its structural integrity. Additionally, to practically realize the tensile strain predicted in our theoretical model, experimental strategies such as A-site cation substitution can be employed. Moreover, strain engineering via heterostructuring or epitaxial growth on substrates with larger lattice constants could also facilitate strain introduction [53,54]. These methods offer promising pathways to experimentally achieve the strain levels required to optimize optoelectronic properties.

Fig. 4 presents the electronic band structure of the studied perovskite $Rb_2NaTlBr_6$ under these tensile strains. The valence band maximum and conduction band minimum both shifted closer to the Fermi level while remaining at the same highest symmetry Γ point. This shift indicates that the compound maintains its electronic aspects with a reduction in the band gap value. Under a tensile strain of −5%, the band gap of the $Rb_2NaTlBr_6$ decreased to approximately 1.374 eV. In addition, the variation in the band gap value with tensile strain is summarized in Table 3. Notably, the band gap energy for $Rb_2NaTlBr_6$ decreased from 1.8 to 1.37 eV with the applied strain, while retaining and keeping its direct band gap feature throughout the entire strain range. These results are significant in the context of the SQ limit, suggesting that material with a direct band gap energy and an optimal band gap value can potentially enhance solar cell efficiency. The ability of $Rb_2NaTlBr_6$ material to maintain a direct band gap while approaching the ideal band gap value makes it a promising candidate for achieving the performance of solar cell. Fig. 5 illustrates the total density of states (TDOS) under tensile strains. It is evident that as tensile strain increases, the band gap energy decreases until a strain 5%, as presented in the band structure (see Fig. 4). Additionally, the TDOS shifts to a lower energy range closer to the Fermi level, verifying and confirming the reduction of the band gap energy of about 1.374 eV. Each applied strain exhibits a similar trend in the unstrained state, with slight variations in the extent of the band gap reduction. This shift of the band gap energy towards the Fermi level suggests that the studied compound approaches the ideal band gap energy, which is particularly significant in the context of the SQ limit.

3.2.4. Carrier transport properties

We assessed the transport behavior of charge carriers in $Rb_2NaTlBr_6$ by calculating the effective masses of electrons (m_e^*) and holes (m_h^*) at the Γ point for both unstrained and strained structures. The effective mass is a crucial parameter affecting carrier mobility, directly associated with the curvature of the electronic bands near the conduction band minimum (CBM) and valence band maximum (VBM). This study computed effective masses utilizing a second-order finite-difference method, employing a parabolic fit to the energy dispersion $E(k)$ in proximity to the Γ point. The effective mass was determined using the conventional formula [55]:

$$m^* = \hbar^2 \left(\frac{d^2 E}{dk^2} \right)^{-1} \tag{5}$$

where m^*, $\hbar$, E, and k are the effective mass, reduced Planck constant, energy, and the wave vector, respectively. The effective mass values are typically normalized to the free electron mass, m_0 providing a dimensionless measure that facilitates comparison between different materials.

The numerical fitting was conducted within a small k-space region around the band extrema, which guaranteed a precise approximation of the curvature. This methodology is commonly employed in studies of perovskite and semiconductor materials, providing reliable estimates of

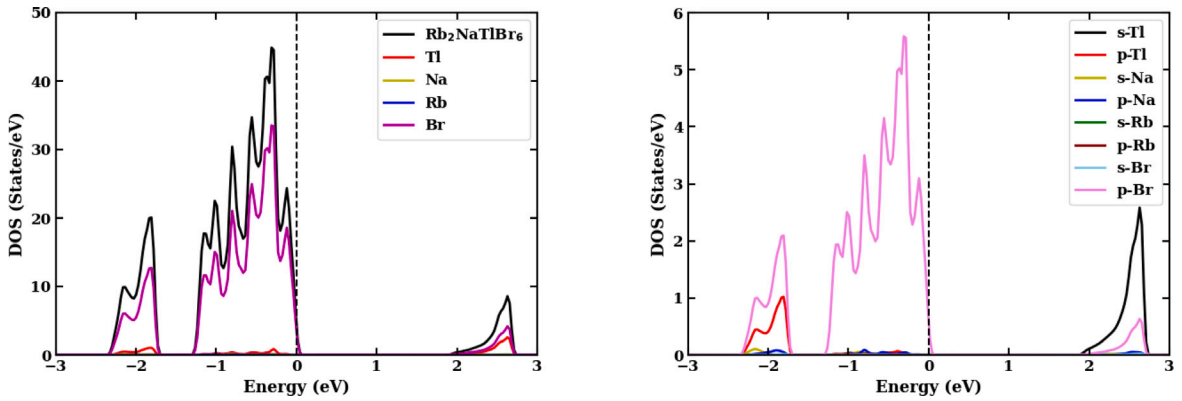

Fig. 3. Total and partial density of states of the $Rb_2NaTlBr_6$ perovskite using PBE+mBJ functional.

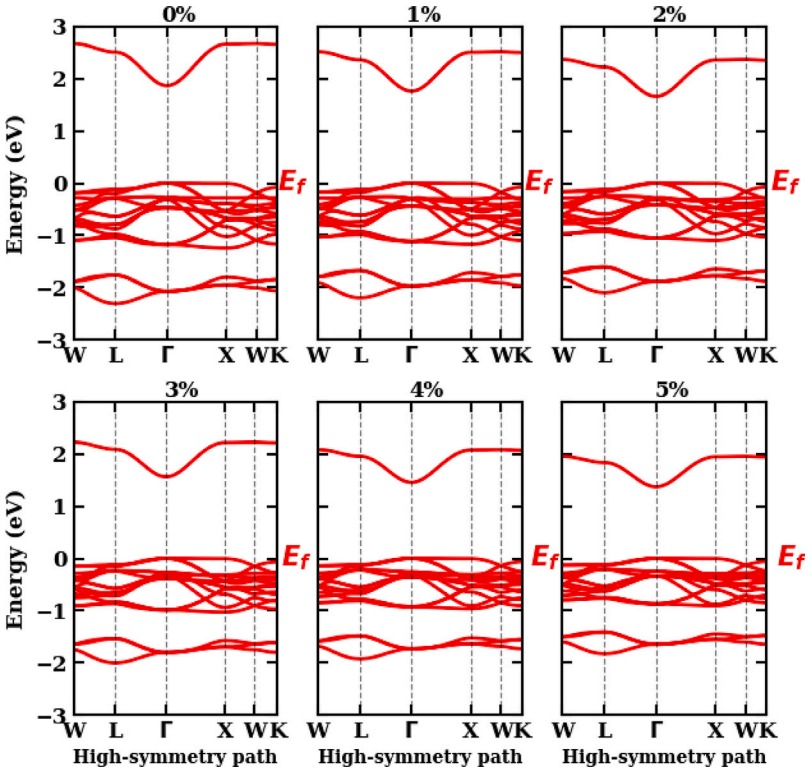

Fig. 4. Electronic band structures of the $Rb_2NaTlBr_6$ perovskite under tensile strain effects using mBJ functional.

charge carrier effective mass, as evidenced by the research conducted by Yin et al. [55]. Fig. 4 shows the computed electron and hole effective masses for $Rb_2NaTlBr_6$ under various tensile strains. The effective masses increase with the applied strain, ranging from 0.1423 to 0.1745 m_e^*/m_0 for electrons and from 0.42 to 0.55 m_h^*/m_0 for holes as the strain varies from 0 to 5%. Although an increase in effective mass generally indicates reduced carrier mobility, this effect must be considered in conjunction with other factors, such as band gap tuning and enhanced absorption characteristics, which are also influenced by strain. Despite the increase in effective masses, they remain relatively low and significant for both electrons and holes, especially in comparison to other perovskite materials including $FAGeCl_3$, $FAPbCl_3$, and $FAPbI_3$ [53,56]. This suggests that the effective masses of $Rb_2NaTlBr_6$ are still favorable for solar cell applications.

The binding energy (E_b) of excitons, representing the Coulomb attraction between electrons and holes, is another critical factor affecting the material's photovoltaic performance. The binding energy can be described by [57]:

$$E_b = 13.56\frac{m_\mu}{m_0}\frac{1}{\varepsilon_1^2(0)} \tag{6}$$

where $\varepsilon_1(0)$ is the static dielectric constant, m_0 is the free electron mass, and m_μ is the decreased effective mass. As shown in Table 4, the binding energy of $Rb_2NaTlBr_6$ increases from 0.196 eV at 0% strain to 0.229

Table 4
Effective masses of holes and electrons, and exciton binding energies for $Rb_2NaTlBr_6$ under varying tensile strains.

Compound	Tensile strain (%)	m_e^*/m_0	m_h^*/m_0	E_b (eV)
$Rb_2NaTlBr_6$	0	0.1423	0.42	0.196
	1	0.1479	0.44	0.203
	2	0.1546	0.45	0.211
	3	0.1613	0.47	0.217
	4	0.1654	0.51	0.221
	5	0.1745	0.55	0.229

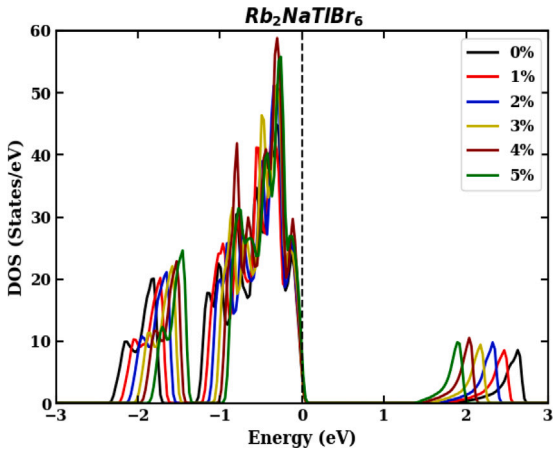

Fig. 5. Total density of states of the $Rb_2NaTlBr_6$ perovskite under tensile strain effects using mBJ functional.

eV at 5% strain. This increase suggests that the electron–hole pairs become more tightly bound under strain. While this stronger binding indicates enhanced exciton stability, it could also hinder charge separation efficiency. Therefore, this hindrance may affect the performance of the studied material in solar cell applications. Engineering type II heterojunctions with appropriate partner materials can effectively facilitate exciton dissociation and improve charge separation. Integrating methylammonium lead iodide ($MAPbI_3$) with fullerene (C_60) creates a heterojunction that enhances electron transfer and minimizes recombination losses [58]. Z.Y. Peng et al. [59] demonstrated that the integration of perovskite with molybdenum disulfide (MoS_2) nanoflakes to create a bulk heterojunction significantly improves photodetector performance. The integration of MoS_2 enables selective electron trapping, thereby inhibiting recombination and enhancing hole transfer to the reduced graphene oxide layer. This design enhances responsivity and detectivity, highlighting the potential of heterojunction engineering to address limitations associated with the high exciton binding energies.

3.3. Optical properties

The fundamental properties related to the semiconductor's band structure are principally detailed through inter and intra-band transitions. The interactions between incident photons and semiconductor materials are explained by the complex dielectric function $\varepsilon(\omega)$, which is expressed as $\varepsilon(\omega) = \varepsilon_1(\omega) + i\varepsilon_2(\omega)$[60]. This research delves into the intricate optical characteristics, including absorption coefficient, refractive index, and reflectivity [61]. The optical properties of $Rb_2NaTlBr_6$ perovskite suggest its significant potential and suitability, particularly for solar cell technologies. Using the tensile strain effects as a method of lattice tuning, the optical behavior of the semiconducting perovskite $Rb_2NaTlBr_6$ can be enhanced. This study investigates the effect of tensile strain ranging from 0 to 5% on various optical properties using mBJ approach.

The complex dielectric function is computed as the sum of the real and imaginary parts. The real part, $\varepsilon_1(\omega)$, represents the material's ability to store energy from the electric field, influencing the dispersion and phase velocity of light within the material [62]. The imaginary part, $\varepsilon_2(\omega)$, describes the material's ability to dissipate energy, determining the absorption of light and its conversion into other forms of energy. Additional optical function, including the absorption coefficient $\alpha(\omega)$, refractive index $n(\omega)$, and reflectivity $R(\omega)$, are given by the following equations [63]:

$$\alpha(\omega) = \frac{\sqrt{2}\omega}{c}\left[\sqrt{\varepsilon_1^2(\omega) + \varepsilon_2^2(\omega)} - \varepsilon_1(\omega)\right]^{1/2}$$

$$n(\omega) = \frac{1}{\sqrt{2}}\left[\sqrt{\varepsilon_1^2(\omega) + \varepsilon_2^2(\omega)} + \varepsilon_1(\omega)\right]^{1/2} \quad (7)$$

$$R(\omega) = \frac{(1-n)^2 + K^2}{(1+n)^2 + K^2}$$

where $K(\omega)$ represents the extinction coefficient, which can be defined as:

$$K(\omega) = \frac{1}{\sqrt{2}}\left[\sqrt{\varepsilon_1^2(\omega) + \varepsilon_2^2(\omega)} - \varepsilon_1(\omega)\right]^{1/2} \quad (8)$$

Fig. 6-(a) depicts the real part of the dielectric function $\varepsilon_1(\omega)$, for both strained and unstrained $Rb_2NaTlBr_6$. For unstrained structure, the static dielectric constant is of about 2.71. This value remains constant until it reaches the first peak around 2.5 eV and the second around 4.3 eV, indicating significant light polarization by the material. Additionally, the unstrain effect on the $Rb_2NaTlBr_6$ exhibits a positive dielectric response throughout the energy range, suggesting high reflectivity and semiconducting aspect [64]. The strain-induced increases the static dielectric constant, as shown in Fig. 6-(b), and shifts the dielectric constant peaks into the visible spectrum. This shift is advantageous for solar cell applications, as it allows the studied material to interact more effectively visible light, improving light absorption and potentially increasing the efficiency of solar cell technologies.

Fig. 6-(c) illustrates the imaginary part of dielectric function $\varepsilon_2(\omega)$, under applied tensile strain. This component is crucial as it represents the amount of energy absorbed by the material when light passes through it and indicates the crystal structure's ability to retain energy from charge excited states. The critical value of $\varepsilon_2(0)$ is approximately at 1.799 eV, corresponding to the optical band gap of $Rb_2NaTlBr_6$. As energy increases, the $\varepsilon_2(\omega)$ shows two prominent peaks around 3 and 4.5 eV, suggesting that $Rb_2NaTlBr_6$ perovskite strongly absorbs the electromagnetic radiation. Under applied tensile strains, the $\varepsilon_2(0)$ value decreases with increasing strain, reflecting a reduction in the band gap energy. Additionally, the imaginary part shifts towards the visible region, indicating an adjustable absorption spectrum. This transition improves the material's overall absorption spectrum, potentially enhancing its efficiency in converting sunlight into electrical energy.

Solar cell applications are closely related to the band gap and absorption coefficient spectra of materials [65]. The absorption coefficient spectra is a key parameter for evaluating a material's ability to absorb light energy, which is crucial for high efficiency solar cell and photovoltaic applications. Fig. 6-(d) shows the absorption coefficient of the $Rb_2NaTlBr_6$ structure as a function of photon energy for both unstrained and strained conditions. The tensile strain affects the band gap energy, moving it closer to the ideal gap value based on the SQ limit, enhancing the absorption coefficient spectrum. This strain-induced shift moves the absorption peaks into the visible light range, allowing the material to absorb light more effectively in this range. The improved absorption coefficient owing to applied tensile strain has the potential to improve the material's efficiency in converting sunlight into electrical energy.

The refractive index, $n(\omega)$, is a crucial physical quantity that provides detailed insight into a material's optical properties, including how it affects light speed and its stability for various device applications. Fig. 6-(e) displays the changes in the refractive index $n(\omega)$ under tensile strain ranging from 0 to 5%. The refractive index exhibits a trend similar to that of $\varepsilon_1(\omega)$. For unstrained $Rb_2NaTlBr_6$, the static refraction index is approximately 1.646. This value increases with the applied strain, as illustrated in Fig. 6-(f). The shift of the refraction index peaks into the visible light range indicates that the material can better reduce the reflection of visible light and enhance its absorption. This improvement contributes to higher efficiency in solar cell applications.

Fig. 6-(g) shows that the reflectivity of $Rb_2NaTlBr_6$ slightly increases from 0.059 to 0.063 as the tensile strain increases from 0 to

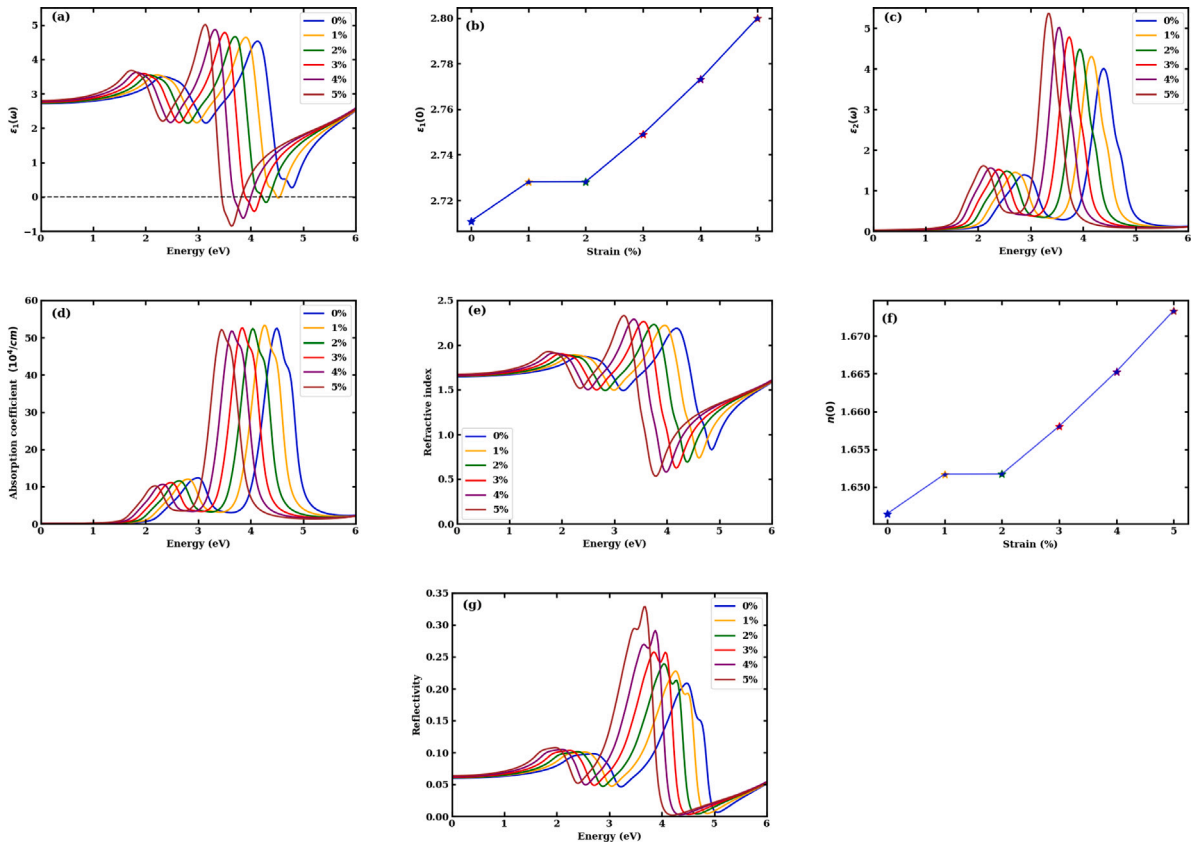

Fig. 6. Optical properties of the material $Rb_2NaTlBr_6$ under various biaxial strain conditions (0%–5%): (a) Real part of the dielectric function $\varepsilon_1(\omega)$, (b) Static dielectric constant $\varepsilon_1(0)$ as a function of strain, (c) Imaginary part of the dielectric function $\varepsilon_2(\omega)$, (d) Absorption coefficient, (e) Refractive index, (f) Static refractive index $n(0)$ as a function of strain, and (g) Reflectivity spectrum.

5%. This change in reflectivity is relevant for solar cell applications, as reflectivity influences how much incident light is absorbed. Although higher reflectivity generally indicates less light absorption, in this case, the overall absorption is actually enhanced. This is primarily due to strain induced band gap narrowing and stronger optical transitions, which together improve light absorption in the visible range. As a result, despite the slight increase in reflectivity, the material demonstrates improved potential for solar energy conversion.

We estimated the surface energy loss function (SELF) and the volume energy loss function (VELF) to evaluate the energy dissipation behavior of fast electrons in the Rb2NaTlBr6 material. These functions were computed using standard relations derived from the complex dielectric function as following [66,67]:

$$\mathrm{SELF} = -\mathrm{Im}\left(\frac{1}{\varepsilon+1}\right) = \frac{\varepsilon_2}{\left(\varepsilon_1+1\right)^2+\varepsilon_2^2} \tag{9}$$

$$\mathrm{VELF} = -\mathrm{Im}\left(\frac{1}{\varepsilon}\right) = \frac{\varepsilon_2}{\varepsilon_1^2+\varepsilon_2^2} \tag{10}$$

Fig. 7 illustrates the energy loss spectra, demonstrating the variation of SELF and VELF as a function of photon energy under different tensile strain levels. The SELF spectra show a notable increase in peak intensity with increasing strain, although the peak resins below 0.95. Similarly, the VELF peak also rises with strain and remains below 1. These findings indicate a low electron energy loss rate, which is beneficial for optoelectronic and photovoltaic applications where reduced energy dissipation is desirable.

3.4. Spectroscopic limited maximum efficiency (SLME)

Theoretically, when selecting suitable materials for solar cells, efficiency calculations precede the first-principles approach. This challenge has been addressed by various prediction models, including the Shockley–Queisser (SQ) model and the Spectroscopic Limited Maximum Efficiency (SLME) model. In this study, we expanded upon the approach developed by Yu and Zunger [68], to calculate the SLME of the $Rb_2NaTlBr_6$ perovskite under various tensile strains to assess its photovoltaic performance. The SLME provides a more comprehensive measure of solar cell efficiency compared to the traditional Shockley–Queisser limit, as it incorporates not only the band gap but also the absorption spectrum and non-radiative recombination losses. The SLME is calculated using the following equation [30]:

$$\eta = \frac{P_m}{P_{in}} \tag{11}$$

The total incident power density of solar radiation, denoted as P_{in}. The maximum power output per unit area of a solar cell, P_m, can be derived from its J-V characteristic, which is used to determine the maximum power density for the SLME:

$$P_m = \max\left(JV\right) = \max\left(\left[J_{sc} - J_0\left(\exp\left(\frac{eV}{K_B T} - 1\right)\right)\right]V\right) \tag{12}$$

In this equation, J represents the current density, V is the voltage across the absorber material, K_B is the Boltzmann constant, T is the temperature, and e is the electron charge. The short-circuit current density J_{sc} and the reverse saturation current density J_0 are calculated as follows:

$$J_{sc} = \int_0^\infty eA(E)I_{sun}dE \tag{13}$$

$$J_0 = \frac{J_0^r}{f_r} = \frac{e\pi}{f_r}\int_0^\infty A(E)I_{bb}(E,T)dE \tag{14}$$

Here, I_{sun} is the photon flux density derived from the AM1.5G spectrum, and I_{bb} is the blackbody spectrum. The term J_0^r refers to the

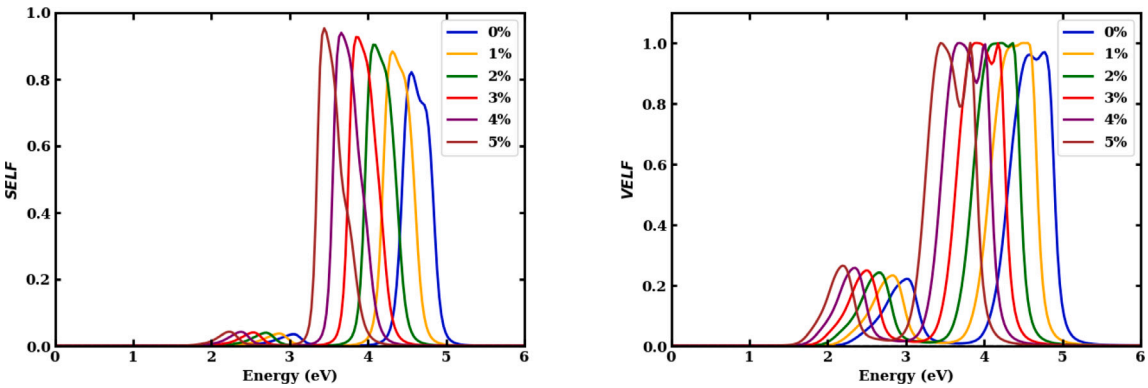

Fig. 7. SELF and VELF functions versus energy of the $Rb_2NaTlBr_6$ perovskite.

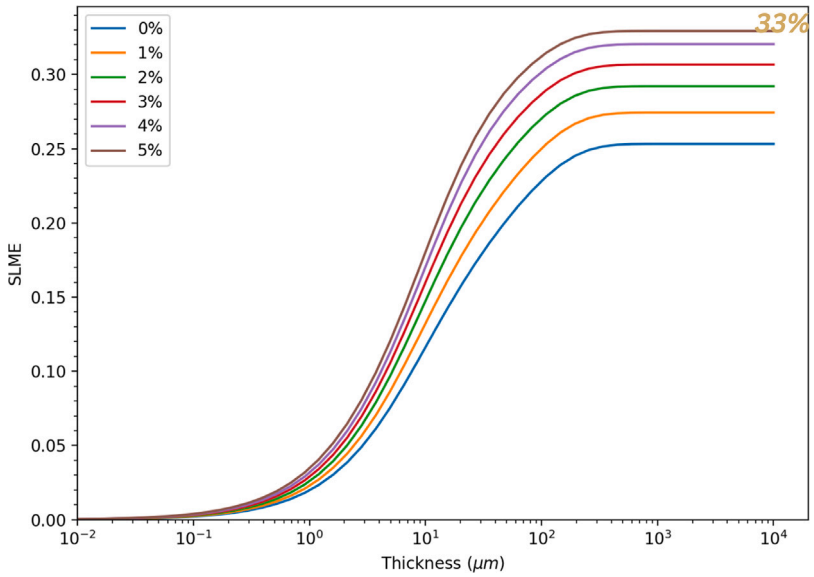

Fig. 8. Theoretical Spectroscopy limited maximum efficiency of $Rb_2NaTlBr_6$ perovskite under tensile strain effects.

radiative recombination current density, and $A(E)$ represents the photon absorptivity of the absorber material. The factor f_r denotes the fraction of the radiative recombination current and is approximated by $f_r = e^{\frac{-\Delta}{K_B T}}$, where $\Delta = E_g^{da} - E_g$, with E_g^{da} and E_g being the direct-allowed and minimum band gap of the material, respectively. For the studied $Rb_2NaTlBr_6$ material, it exhibits a direct band gap, meaning $E_g = E_g^{da}$. Consequently, only radiative recombination is considered, and therefore $f_r = 1$.

The Spectroscopic Limited Maximum Efficiency (SLME) of $Rb_2NaTlBr_6$ was calculated across a range of tensile strains from 0 to 5%, revealing a significant impact on the material's photovoltaic efficiency, as shown in Fig. 8. At 0% strain, the SLME was approximately 25%. With increasing tensile strain, the band gap decreased, enhancing photon absorption and resulting in a corresponding rise in SLME. The SLME reached its peak at around 33% under 5% strain, demonstrating a notable improvement over the unstrained material. This improvement is attributed to the strain-induced optimization of the band gap, bringing it closer to the ideal range for photovoltaic applications. Additionally, the SLME was evaluated as a function of material thickness, spanning from 10^{-2} to 10^4 micrometers, as depicted in Fig. 8. These results suggest that strain engineering, coupled with optimal material thickness, can significantly enhance the efficiency of $Rb_2NaTlBr_6$, positioning it as a strong candidate for high-performance, lead-free perovskite solar cells.

4. Conclusion

In this work, we present the first comprehensive theoretical investigation of the photovoltaic potential of the double halide perovskite $Rb_2NaTlBr_6$, employing state-of-the-art density functional theory calculations implemented in the WIEN2k code. Our systematic analysis reveals that $Rb_2NaTlBr_6$ exhibits remarkable structural stability and favorable semiconducting characteristics, featuring a direct band gap that is ideal for photovoltaic applications. Through strategic application of strain engineering, we successfully optimized the band gap while preserving the direct transition nature, resulting in significantly enhanced optical absorption and charge transport properties. Most notably, our calculations predict a SLME of 33%, substantially exceeding the theoretical efficiencies reported for many existing halide perovskite materials. The combination of structural stability, optimized electronic structure, and exceptional theoretical efficiency positions $Rb_2NaTlBr_6$ as a highly promising candidate for next-generation photovoltaic devices. These findings not only establish $Rb_2NaTlBr_6$ as a potential breakthrough material for solar cell applications, but also provide valuable insights for the rational design of high-performance double halide perovskites. Future experimental investigations of this material system could potentially validate these theoretical predictions and pave the way for practical implementation in efficient photovoltaic devices.

CRediT authorship contribution statement

M. Agouri: Writing – original draft, Software, Investigation, Conceptualization. **H. Fatihi:** Writing – original draft, Data curation, Conceptualization. **H. Ouhenou:** Writing – original draft, Software, Conceptualization. **N. Khossossi:** Writing – review & editing, Software, Investigation. **A. Abbassi:** Writing – review & editing, Supervision, Investigation. **S. Taj:** Visualization, Validation, Supervision. **B. Manaut:** Validation, Supervision.

Declaration of competing interest

The authors declare that they have no known competing financial interests or personal relationships that could have appeared to influence the work reported in this paper.

Data availability

Data will be made available on request.

References

[1] A. Manberger, Biophys. Econ. Sust. 6 (2021) 6.
[2] Q. Hassan, et al., Renew. Energy Focus. 48 (2024) 100545, http://dx.doi.org/10.1016/j.ref.2024.100545.
[3] M.L. Petrus, et al., Adv. Energy Mater. 7 (2017) 1700264, http://dx.doi.org/10.1002/aenm.201700264.
[4] A.O.M. Maka, et al., Clean. Eng. Technol. 5 (2021) 100267, http://dx.doi.org/10.1016/j.clet.2021.100267.
[5] N.A. Ludin, et al., Renew. Sustain. Energy Rev. 96 (2018) 11–28, http://dx.doi.org/10.1016/j.rser.2018.07.048.
[6] N. Kumar, et al., Mater. Today Proc. 46 (2021) 5570–5574, http://dx.doi.org/10.1016/j.matpr.2020.09.349.
[7] H. Ouhenou, et al., Radiat. Meas. 177 (2024) 107228, http://dx.doi.org/10.1016/j.radmeas.2024.107228.
[8] S. Nair, et al., Mater. Today Energy 17 (2020) 100449, http://dx.doi.org/10.1016/j.mtener.2020.100449.
[9] J. Chen, et al., J. Power Sources 355 (2017) 98–133, http://dx.doi.org/10.1016/j.jpowsour.2017.04.025.
[10] M.A. Green, et al., Prog. Photovolt. 31 (2023) 3–16, http://dx.doi.org/10.1002/pip.3646.
[11] A. Kojima, et al., J. Am. Chem. Soc. 131 (2009) 6050–6051, http://dx.doi.org/10.1021/ja809598r.
[12] H. Wei, et al., Ceram. Int. 48 (2022) 5876, http://dx.doi.org/10.1016/j.ceramint.2021.11.184.
[13] X. Qiu, et al., Sol. Energy Mater. Sol. Cells 159 (2017) 227–234, http://dx.doi.org/10.1016/j.solmat.2016.09.022.
[14] A. Babayigit, et al., Sci. Rep. 6 (2016) 18721, http://dx.doi.org/10.1038/srep18721.
[15] F. Temerov, et al., ACS Appl. Energy Mater. 5 (2022) 14605–14637, http://dx.doi.org/10.1021/acsaem.2c02680.
[16] X. Wang, et al., Mater. Chem. Front. 3 (2019) 365–375, http://dx.doi.org/10.1039/C8QM00611C.
[17] M.S. Shadabroo, et al., Mater. Sci. Semicond. 125 (2021) 105639, http://dx.doi.org/10.1016/j.mssp.2020.105639.
[18] M. Agouri, et al., Eur. Phys. J. B 97 (2024) 27, http://dx.doi.org/10.1140/epjb/s10051-024-00663-x.
[19] A.K. Jena, et al., Chem. Rev. 119 (2019) 3036–3103, http://dx.doi.org/10.1021/acs.chemrev.8b00539.
[20] A.T. Barrows, et al., Energy Env. Sci. 7 (2014) 2944–2950, http://dx.doi.org/10.1039/C4EE01546K.
[21] M. Grätzel, Nat. Mater. 13 (2014) 838–842, http://dx.doi.org/10.1038/nmat4065.
[22] M.R. Filip, et al., J.Phys. Chem. Lett. 13 (2016) 2579–2585, http://dx.doi.org/10.1021/acs.jpclett.6b01041.
[23] V. Kumar, et al., Nano Energy 125 (2024) 109523, http://dx.doi.org/10.1016/j.nanoen.2024.109523.
[24] A. Bala, et al., Phys. Rev. Mater. 5 (2021) 095401, http://dx.doi.org/10.1103/PhysRevMaterials.5.095401.
[25] A.H. Slavney, et al., J. Am. Chem. Soc. 138 (2016) 2138–2141, http://dx.doi.org/10.1021/jacs.5b13294.
[26] M. Caid, et al., Comput. Condens. Matter 41 (2024) e00978, http://dx.doi.org/10.1016/j.cocom.2024.e00978.
[27] M.A. Rehman, et al., Phys. B Condens. Matter. 695 (2024) 416499, http://dx.doi.org/10.1016/j.physb.2024.416499.
[28] T.S. Ahmad, et al., Results Phys. 63 (2024) 107885, http://dx.doi.org/10.1016/j.rinp.2024.107885.
[29] M. Delor, et al., ACS Energy Lett. 5 (2020) 1337–1345, http://dx.doi.org/10.1021/acsenergylett.0c00414.
[30] H. Fatihi, et al., J. Inorg. Organomet. Polym. (2024) http://dx.doi.org/10.1007/s10904-024-03330-x.
[31] M. Batouche, et al., Mater. Res. Express 7 (1) (2020) 016305, http://dx.doi.org/10.1088/2053-1591/ab6254.
[32] E.K.U. Gross, et al., Density functional theory, 1993, http://dx.doi.org/10.1007/978-1-4757-9975-0.
[33] P. Blaha, et al., J. Chem. Phys. 152 (2020) 074101, http://dx.doi.org/10.1063/1.5143061.
[34] J.P. Perdew, et al., Phys. Rev. Lett. 78 (1997) 1396, http://dx.doi.org/10.1103/PhysRevLett.77.3865.
[35] D. Koller, et al., PRB 85 (2012) 155109, http://dx.doi.org/10.1103/PhysRevB.85.155109.
[36] K. Kurita, et al., PRB 102 (2020) 045109, http://dx.doi.org/10.1103/PhysRevB.102.045109.
[37] F. Tran, et al., Phys. Rev. Lett. 102 (2009) 226401, http://dx.doi.org/10.1103/PhysRevLett.102.226401.
[38] F. Tran, et al., J. Phys.: Condens. Matter. 19 (2007) 196208, http://dx.doi.org/10.1088/0953-8984/19/19/196208.
[39] B. Yang, Chem. Soc. Rev. 51 (2022) 7509–7530, http://dx.doi.org/10.1039/D2CS00278G.
[40] A. Ayyaz, et al., Phys. Rev. B Condens. 690 (2024) 416245, http://dx.doi.org/10.1016/j.physb.2024.416245.
[41] M. Zia ur Rehman, et al., Mater. Sci. Semicond. Process. 151 (2022) 106993, http://dx.doi.org/10.1016/j.mssp.2022.106993.
[42] A. Ayyaz, et al., JMPS 4 (2023) 92–101, http://dx.doi.org/10.52131/jmps.2023.0402.0039.
[43] L. Zhang, et al., Nano-Micro Lett. 15 (2023) 177, http://dx.doi.org/10.1007/s40820-023-01140-3.
[44] V.M. Goldschmidt, et al., Naturwissenschaften 14 (1926) 477–485, http://dx.doi.org/10.1007/BF01507527.
[45] C. Li, et al., Acta Crystallogr. B. 64 (2008) 702–707, http://dx.doi.org/10.1107/s0108768108032734.
[46] C.J. Bartel, et al., Sci. Adv. 5 (2019) eaav0693, http://dx.doi.org/10.1126/sciadv.aav0693.
[47] E. Meyer, et al., Metals 8 (2018) 667, http://dx.doi.org/10.3390/met8090667.
[48] H. Md. Miah, et al., RSC Adv. 14 (2024) 15876–15906, http://dx.doi.org/10.1039/D4RA01640H.
[49] A. Boutramine, et al., Opt. Quantum Electron. 56 (2024) 417, http://dx.doi.org/10.1007/s11082-024-06344-4.
[50] S. Ruhle, Sol. Energy 130 (2016) 139–147, http://dx.doi.org/10.1016/j.solener.2016.02.015.
[51] S. Tariq, et al., Heliyon 10 (2024) e40315, http://dx.doi.org/10.1016/j.heliyon.2024.e40315.
[52] B. Rezini, et al., Int. J. Quantum Chem. 122 (2022) e26977, http://dx.doi.org/10.1002/qua.26977.
[53] C. Yimu, et al., Nature 577 (7789) (2020) 209–215, http://dx.doi.org/10.1038/s41586-019-1868-x.
[54] M. Wang, et al., Chem. Phys. Rev. 2 (2021) 031302, http://dx.doi.org/10.1063/5.0044588.
[55] W.J. Yin, et al., J. Mater. Chem. A 3 (2015) 8926–8942, http://dx.doi.org/10.1039/C4TA05033A.
[56] Md. Roknuzzaman, et al., Comput. Mater. Sci. 169 (2019) 109118, http://dx.doi.org/10.1016/j.commatsci.2019.109118.
[57] U.J. Jong, et al., PRB 94 (2016) 125139, http://dx.doi.org/10.1103/PhysRevB.94.125139.
[58] K.H. Chew, et al., Mater. Adv. 2 (2021) 1665–1675, http://dx.doi.org/10.1039/D0MA00853B.
[59] Z.Y. Peng, et al., Adv. Mater. Interfaces 5 (2018) 1800505, http://dx.doi.org/10.1002/admi.201800505.
[60] Z. Xu, Solid State Commun. 76 (1990) 1143–1147, http://dx.doi.org/10.1016/0038-1098(90)90981-G.
[61] K.E. Peiponen, et al., Eur. Phys. J. B 41 (2004) 61–65, http://dx.doi.org/10.1140/epjb/e2004-00294-6.
[62] M. Fox, Optical Properties of Solids, vol. 3, Oxford University Press, 2010.
[63] M. Dresselhaus, et al., Solid state properties, 2018, http://dx.doi.org/10.1007/978-3-662-55922-2.
[64] M.F.I. Buian, et al., Mater. Sci. Semicond. Process. 180 (2024) 108580, http://dx.doi.org/10.1016/j.mssp.2024.108580.
[65] T. Zdanowicz, et al., Sol. Energy Mater. Sol. Cells 87 (2005) 757–769, http://dx.doi.org/10.1016/j.solmat.2004.07.049.
[66] W. Ouerghui, et al., Opt. Quantum Electron. 56 (2024) 354, http://dx.doi.org/10.1007/s11082-023-05866-7.
[67] M. Batouche, et al., Mat. Sci. Semicon. Proc. 164 (2023) 107600, http://dx.doi.org/10.1016/j.mssp.2023.107600.
[68] L. Yu, et al., PRL 108 (2012) 068701, http://dx.doi.org/10.1103/PhysRevLett.108.068701.